

Extracting phase coupling functions between networks of dynamical elements that exhibit collective oscillations: Direct extraction from time-series data

Takahiro Arai,^{1,*} Yoji Kawamura,² and Toshio Aoyagi¹

¹*Graduate School of Informatics, Kyoto University,
Yoshida-Honmachi, Sakyo-ku, Kyoto 606-8501, Japan*

²*Center for Mathematical Science and Advanced Technology,
Japan Agency for Marine-Earth Science and Technology, Yokohama 236-0001, Japan*

(Dated: November 1, 2021)

Many real-world systems are often regarded as weakly coupled limit-cycle oscillators, in which each oscillator corresponds to a dynamical system with a large number of degrees of freedom exhibiting collective oscillations. One of the most practical methods for investigating the synchronization properties of such a rhythmic system is to statistically extract phase coupling functions between limit-cycle oscillators directly from observed time-series data. Particularly, using the method that combines phase reduction theory and Bayesian inference, the phase coupling functions can be extracted even from the time-series data of only one variable in each oscillatory dynamical system with many degrees of freedom. However, it remains unclear how the choice of the observed variables affects the statistical inference for the phase coupling functions. In this study, we examine the influence of observed variable types on the extraction of phase coupling functions using some typical dynamical elements under various conditions. Thus, we demonstrate that our method can consistently extract the macroscopic phase coupling functions between two phases representing collective oscillations regardless of the observed variable types, e.g., even when using one variable of any element in one system and the mean-field value over all the elements in another system.

I. INTRODUCTION

Synchronization phenomena of coupled dynamical elements are known in many fields, such as biological and engineering systems, and often play important roles [1]. Further, collective synchronization has been widely studied not only for globally coupled systems but also for complex network systems [2–5]. The framework to derive a low-dimensional description of the dynamics has been developed to analyze these collective dynamics. One of the most successful and widely used theoretical methods is the phase reduction theory [6–16]. This method derives the phase description, in which the dynamics at the vicinity of the limit-cycle is projected onto a single phase equation, such that the interaction between oscillators can be simply described as a phase coupling function.

Recently, statistical methods to extract the phase coupling function directly from observed time-series have been developed: the methods to reconstruct phase dynamics of two oscillators [17, 18], effective connectivity of an oscillator network [19, 20], phase coupling function [21], and phase sensitivity function [22–26]. Further, several methods employing the Bayesian inference framework [27] have also been proposed to extract the phase description [28–31]. These methods have been used in various situations: choruses of frogs [32], electroencephalography [33–36], and spiking neurons [37].

In general, real-world systems are comprised of many interacting subsystems, in which each subsystem is also comprised of many elements and exhibits collective dynamics. These subsystems often interact with each other

to coordinate their functional activities. For example, each brain region exhibits synchronous oscillation dynamics of the neural population, and the synchronization of those oscillations between brain regions has been studied as the effective connectivity [38, 39]. The effective connectivity has been widely studied for the resting-state of the human brain [40], epileptic seizures [41, 42], and cognition and working memory [43]. Both theory and inference methods for coupling functions between subsystems are significant in neuroscience since the brain's architecture is a highly connected complex system [44].

Here, we consider a dynamical system that consists of networks of dynamical elements. The model reduction for collective dynamics has been intensively investigated for analyzing the macroscopic synchronization properties between each network that shows collective dynamics [45–51]. Moreover, several theoretical frameworks to reduce the collective dynamics to a single phase variable have been developed [52–59]. Using these methods, thus, we can investigate a macroscopic phase sensitivity function and a macroscopic phase coupling function between networks. Figure 1(a) illustrates the framework developed in Ref. [59], where two networks exhibiting collective oscillations have many internal and external couplings. In this case, the dynamics of the entire network is reduced to a one-dimensional phase equation, and the derived phase coupling function describes the effect of all the external couplings between two networks on the phase dynamics. Although analytical studies have been conducted, inference methods for the collective dynamics are yet to be fully investigated.

In this study, to extract the macroscopic phase coupling functions between networks, we extend the range of the Bayesian inference method applications [31] from

* arai@acs.i.kyoto-u.ac.jp

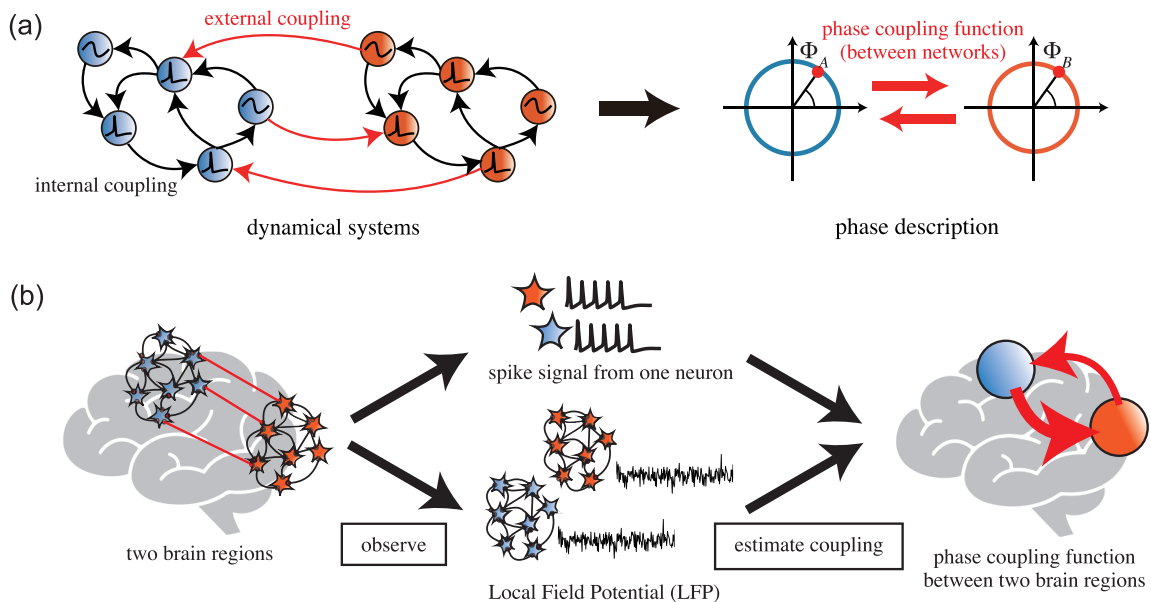


FIG. 1. Schematic diagrams of the phase reduction method for collective oscillation and the statistical inference of phase coupling function. (a) Schematic diagram of the phase reduction method for collective oscillation. The left figure shows that, each network has many elements, and internal couplings (black arrows) and external couplings (red arrows) exist. When each network has a stable limit-cycle and the external couplings are sufficiently weak, the dynamics of each network can be projected onto a single phase equation, and the phase coupling function between the networks (red arrows) can be derived as a simple form, as illustrated in the right figure. (b) Schematic diagram of statistical inference of the connectivity between brain regions. The dynamics of one brain region, which is a neural population, can be observed as spike signals of one neuron, Local Field Potential (LFP), and so on. The phase coupling function is extracted from observed time-series, however, the same results may not necessarily be obtained from two observation methods.

a phase representing the state of one element to a macroscopic phase representing the state of an entire network exhibiting collective oscillation [59]. The phase coupling function can be extracted from the time-series of only one variable by introducing the phase description into the statistical inference method. Note that it is sufficient to observe time-series of only one variable of each network exhibiting collective oscillation, not all the variables. Here, let us consider an example shown in Fig. 1(b), where the purpose is to analyze the macroscopic phase coupling functions between two brain regions from observed time-series data. Most studies have supposed that these coupling functions are extracted from the Local Field Potential (LFP) time-series, which reflect the activities of neural populations. However, it is unclear what the coupling function extracted from the time-series of the spike signals of one neuron represents. Moreover, the extraction of coupling functions may also be affected by the choice of elements for observation, e.g., an excitatory or inhibitory neuron can be chosen.

In this study, we evaluate the effect of the choice of observed variables on the extraction of the phase coupling function. In Sec. II, we briefly review the phase reduction method for collective oscillation and the Bayesian inference method for extracting the phase description directly

from time-series data. In Sec. III, we apply the method to extract the interaction between networks for two networks of FitzHugh-Nagumo (FHN) elements (Sec. III A), three networks of FHN elements (Sec. III B), and two networks of van der Pol oscillators (Sec. III C). In those cases, three types of observed variables are studied: one excitable element, one oscillatory element, and mean-field. In Sec. IV, we discuss the method's implications for the characterization of the interaction between networks directly from time-series data.

II. METHODS

In this section, we briefly review both the phase description for collective oscillations (Sec. II A) and the Bayesian framework to extract the collective phase description directly from time-series data (Sec. II B).

A. Phase description

We consider N networks of coupled dynamical elements and weak interactions between the networks. The dynamics of element i ($i = 1, 2, \dots, N_\gamma$) in network γ is

given by

$$\begin{aligned} \frac{d}{dt} \mathbf{X}_i^\gamma(t) = & \mathbf{F}_i^\gamma(\mathbf{X}_i^\gamma(t)) + \sum_{j \neq i}^{N_\gamma} \mathbf{G}_{ij}^\gamma(\mathbf{X}_i^\gamma(t), \mathbf{X}_j^\gamma(t)) \\ & + \epsilon \sum_{\nu \neq \gamma} \sum_{j=1}^{N_\nu} \mathbf{H}_{ij}^{\gamma\nu}(\mathbf{X}_i^\gamma(t), \mathbf{X}_j^\nu(t)) + \boldsymbol{\eta}_i^\gamma(t), \end{aligned} \quad (1)$$

where $\mathbf{X}_i^\gamma(t) \in \mathbf{R}^{d_i^\gamma}$ represents the d_i^γ -dimensional state of element i in network γ at time t , $\mathbf{F}_i^\gamma : \mathbf{R}^{d_i^\gamma} \rightarrow \mathbf{R}^{d_i^\gamma}$ represents the individual dynamics of element i in network γ , and $\mathbf{G}_{ij}^\gamma : \mathbf{R}^{d_i^\gamma} \times \mathbf{R}^{d_j^\gamma} \rightarrow \mathbf{R}^{d_i^\gamma}$ represents the internal coupling from element j to element i in network γ . We assume that self-coupling does not exist or is absorbed into the individual dynamics term \mathbf{F}_i^γ , i.e., $\mathbf{G}_{ii}^\gamma = \mathbf{0}$. In this system, there are external couplings between elements belonging to different networks as $\mathbf{H}_{ij}^{\gamma\nu} : \mathbf{R}^{d_i^\gamma} \times \mathbf{R}^{d_j^\nu} \rightarrow \mathbf{R}^{d_i^\gamma}$. The intensity of the external couplings is determined by ϵ . Independent white Gaussian noise $\boldsymbol{\eta}_i^\gamma \in \mathbf{R}^{d_i^\gamma}$ is given to each element in each network.

We introduce the phase description into the dynamical system described by Eq. (1). Here, we assume that each network exhibits collective oscillation, and that there are no perturbations to them, i.e., $\epsilon = 0$ and $\boldsymbol{\eta}_i^\gamma = \mathbf{0}$. Under this condition, the dynamics of element i in network γ is assumed to exhibit periodic oscillation as follows:

$$\mathbf{X}_i^\gamma(t) = \mathbf{X}_i^\gamma(t + T_\gamma), \quad (2)$$

where each network possesses a stable limit-cycle solution. In this situation, all the elements in network γ exhibit periodic oscillation with the period T_γ . Let us consider the phase variable $\Phi_\gamma(t) \in [0, 2\pi)$. The state of network γ at time t can be described as a function of the phase variable, i.e., $\mathbf{X}_i^\gamma(t) = \mathbf{X}_i^\gamma(\Phi_\gamma(t))$, where the value of Φ_γ indicates the state of network γ , which is in the vicinity of the limit-cycle. Without any perturbations, the phase variable, $\Phi_\gamma(t)$, is expected to increase with a constant natural frequency Ω_γ as follows:

$$\frac{d}{dt} \Phi_\gamma(t) = \Omega_\gamma, \quad (3)$$

where $\Omega_\gamma := 2\pi/T_\gamma$.

We now consider a case in which perturbation to each network is given but the perturbation intensity is so weak that the collective oscillation persists. To satisfy this condition, the intensity of external couplings between networks is set to $\epsilon \ll 1$, and the noise intensity, $\boldsymbol{\eta}_i^\gamma$, is also assumed to be small. The effect of the perturbation appears on the phase variable in this situation. The dynamics of each network described by Eq. (1) can be reduced to the following phase equation using the phase description:

$$\frac{d}{dt} \Phi_\gamma(t) = \Omega_\gamma + \epsilon \sum_{\nu \neq \gamma} \Gamma_{\gamma\nu}(\Delta\Phi_{\gamma\nu}) + \xi_\gamma(t), \quad (4)$$

where $\Delta\Phi_{\gamma\nu} := \Phi_\nu - \Phi_\gamma$ is the phase difference between networks γ and ν , and $\Gamma_{\gamma\nu}(\Delta\Phi_{\gamma\nu})$ is the phase coupling function from network ν to network γ . The independent white Gaussian noise $\xi_\gamma(t)$ given to network γ satisfies $\langle \xi_\gamma(t) \rangle = 0$ and $\langle \xi_\gamma(t) \xi_\nu(s) \rangle = 2D_\gamma \delta_{\gamma\nu} \delta(t-s)$, where $\delta_{\gamma\nu}$ and $\delta(t)$ are the Kronecker delta and Dirac delta functions, respectively. Note that the phase coupling function, $\Gamma_{\gamma\nu}(\Delta\Phi_{\gamma\nu})$, which depends only on the phase difference, $\Delta\Phi_{\gamma\nu}$, represents the effect of all the external couplings $\mathbf{H}_{ij}^{\gamma\nu}(\mathbf{X}_i^\gamma(\Phi_\gamma), \mathbf{X}_j^\nu(\Phi_\nu))$ from network ν to network γ . Further, $\xi_\gamma(t)$ represents the effect of all $\boldsymbol{\eta}_i^\gamma(t)$ given to network γ .

Because the phase coupling function $\Gamma_{\gamma\nu}(\Delta\Phi_{\gamma\nu})$ is a 2π -periodic function, it can be expanded as a Fourier series

$$\begin{aligned} \Gamma_{\gamma\nu}(\Delta\Phi_{\gamma\nu}) = & a_{\gamma\nu}^{(0)} + \sum_{m=1}^{M_{\gamma\nu}} \left(a_{\gamma\nu}^{(m)} \cos(\Delta\Phi_{\gamma\nu}) \right. \\ & \left. + b_{\gamma\nu}^{(m)} \sin(\Delta\Phi_{\gamma\nu}) \right), \end{aligned} \quad (5)$$

where the phase coupling function, $\Gamma_{\gamma\nu}(\Delta\Phi_{\gamma\nu})$, has been expanded up to $M_{\gamma\nu}$ th order. The maximum order $M_{\gamma\nu}$ is determined from the model selection (Sec. II B). To eliminate the redundancy of the two constant terms, $a_{\gamma\nu}^{(0)}$ and Ω_γ , we define $\hat{\Omega}_\gamma := \Omega_\gamma + \epsilon \sum_{\nu \neq \gamma} a_{\gamma\nu}^{(0)}$ and $\hat{\Gamma}_{\gamma\nu}(\Delta\Phi_{\gamma\nu}) := \Gamma_{\gamma\nu}(\Delta\Phi_{\gamma\nu}) - a_{\gamma\nu}^{(0)}$.

B. Extraction of phase description directly from time-series data

The Bayesian inference method [31] is used to extract the phase dynamics described by Eq. (4) directly from phase time-series data $\{\Phi_\gamma(t_l)\}_{\gamma,l}$ ($l = 0, 1, \dots, L$). In the model identification for the phase dynamics of network γ , we estimate the parameters $\hat{\Omega}_\gamma$, $\{a_{\gamma\nu}^{(1)}, b_{\gamma\nu}^{(1)}, \dots, a_{\gamma\nu}^{(M_{\gamma\nu})}, b_{\gamma\nu}^{(M_{\gamma\nu})}\}_\nu$, and $\hat{D}_\gamma := 2D_\gamma/\Delta t$, where Δt is the sampling interval of the phase time-series.

We denote the phase time-series as $\{\Phi(t)\}$ instead of $\{\Phi_\gamma(t_l)\}_{\gamma,l}$ for simplicity, and we also use the following shorthand notation:

$$\begin{aligned} \mathbf{c}_\gamma &:= (\hat{\Omega}_\gamma, \mathbf{c}_{\gamma,1}, \dots, \mathbf{c}_{\gamma,\gamma-1}, \mathbf{c}_{\gamma,\gamma+1}, \dots, \mathbf{c}_{\gamma,N})^\top, \\ \mathbf{c}_{\gamma,\nu} &:= (a_{\gamma\nu}^{(1)}, b_{\gamma\nu}^{(1)}, \dots, a_{\gamma\nu}^{(M_{\gamma\nu})}, b_{\gamma\nu}^{(M_{\gamma\nu})}). \end{aligned}$$

We define the likelihood function as follows:

$$\begin{aligned} & P(\{\Phi(t)\} | \mathbf{c}_\gamma, \hat{D}_\gamma) \\ &= \prod_{l=0}^{L-1} \mathcal{N} \left(\dot{\Phi}_\gamma(t_l) \middle| \hat{\Omega}_\gamma + \epsilon \sum_{\nu \neq \gamma} \hat{\Gamma}_{\gamma\nu}(\Delta\Phi_{\gamma\nu}(t_l)), \hat{D}_\gamma \right), \end{aligned} \quad (6)$$

where the Gaussian distribution corresponds to model fitting of the nonlinear equation, i.e., Eq. (4). The phase derivative is evaluated as $\dot{\Phi}_\gamma(t_l) := \frac{\Phi_\gamma(t_{l+1}) - \Phi_\gamma(t_l)}{t_{l+1} - t_l}$.

We adopt a Gaussian-inverse-gamma distribution for the conjugate prior distribution, as follows:

$$P_{\text{prior}}(\mathbf{c}_\gamma, \hat{D}_\gamma) = \mathcal{N}(\mathbf{c}_\gamma | \boldsymbol{\chi}_0, \hat{D}_\gamma \Sigma_0) \mathcal{IG}(\hat{D}_\gamma | \alpha_0, \beta_0) \quad (7)$$

where $\boldsymbol{\chi}_0$, Σ_0 , α_0 , and β_0 are the hyperparameters. In this study, we consider $\boldsymbol{\chi}_0 := \mathbf{0}$ and $\Sigma_0 := \lambda_0^{-1} \mathbf{I}$, where \mathbf{I} is an identity matrix. We can easily calculate the posterior distribution of \mathbf{c}_γ and \hat{D}_γ as follows:

$$P_{\text{post}}(\mathbf{c}_\gamma, \hat{D}_\gamma | \{\Phi(t)\}) \propto P(\{\Phi(t)\} | \mathbf{c}_\gamma, \hat{D}_\gamma) \times P_{\text{prior}}(\mathbf{c}_\gamma, \hat{D}_\gamma). \quad (8)$$

The model complexity depends on $M_{\gamma\nu}$, which determines the dimensionality of \mathbf{c}_γ and the maximum order of the Fourier series, as shown in Eq. (5). We determine $M_{\gamma\nu}$ by choosing the value of $M'_{\gamma\nu} \in \mathbf{Z}$ ($0 \leq M'_{\gamma\nu} \leq M_{\text{max}}$), which maximizes the model evidence $P_{\text{ME}}(\{\Phi(t)\} | M'_{\gamma\nu})$ as follows:

$$M_{\gamma\nu} = \arg \max_{0 \leq M'_{\gamma\nu} \leq M_{\text{max}}} P_{\text{ME}}(\{\Phi(t)\} | M'_{\gamma\nu}), \quad (9)$$

$$P_{\text{ME}}(\{\Phi(t)\} | M'_{\gamma\nu}) = \frac{P(\{\Phi(t)\} | \mathbf{c}_\gamma, \hat{D}_\gamma) P_{\text{prior}}(\mathbf{c}_\gamma, \hat{D}_\gamma)}{P_{\text{post}}(\mathbf{c}_\gamma, \hat{D}_\gamma | \{\Phi(t)\})}.$$

In this study, we define $M_{\text{max}} := 15$ and all $M_{\gamma\nu}$ are determined in the range of less than M_{max} .

III. RESULTS

The following three cases are considered in this section: two networks of FHN elements (Sec. III A), three networks of FHN elements (Sec. III B), and two networks of van der Pol oscillators (Sec. III C). In each case, we first explain the dynamics of a system and how to obtain phase time-series from observed time-series. Second, we show a representative result of our method. Finally, we examine the effect of the choice of observed variables on the result of our method.

A. Case 1: Two networks of FHN elements

We consider a case of two ($N = 2$) FHN networks exhibiting collective oscillations. Figure 2(a) shows that networks A and B interact with each other. The state variable of each element in network γ is represented by $\mathbf{X}_i^\gamma = (u_i^\gamma, v_i^\gamma)$ ($i = 1, 2, \dots, 10$), which follows

$$\dot{u}_i^\gamma = \delta^\gamma (a + v_i^\gamma - bu_i^\gamma), \quad (10)$$

$$\dot{v}_i^\gamma = v_i^\gamma - \frac{(v_i^\gamma)^3}{3} - u_i^\gamma + I_i + \sum_{j \neq i}^{10} K_{ij}^\gamma (v_j^\gamma - v_i^\gamma) + \epsilon \sum_{j=1}^{10} C_{ij}^{\gamma\nu} (v_j^\nu - v_i^\gamma) + \eta_i^\gamma(t), \quad (11)$$

where $(\gamma, \nu) = (A, B), (B, A)$. The value of $K_{ij}^\gamma \in \mathbf{R}$ determines the intensity of the internal coupling from element j to element i in network γ , and the set $\{K_{ij}^\gamma\}_{i,j}$ determines the structure of network γ . The connection from element j in network ν to element i in network γ is determined by $C_{ij}^{\gamma\nu} \in \{0, 1\}$. Each element can be oscillatory or excitable depending on the value of the parameter I_i . Each value is $I_i = 0.2$ for $i = 1, \dots, 7$, which exhibits excitable dynamics, and $I_i = 0.8$ for $i = 8, 9, 10$, which exhibits oscillatory one. The time constants are set to $\delta^A = 0.08$ and $\delta^B = 0.073$. The other parameters are $a = 0.7$ and $b = 0.8$. The Gaussian noise $\eta_i^\gamma(t)$ satisfies $\langle \eta_i^\gamma(t) \rangle = 0$, $\langle \eta_i^\gamma(t) \eta_j^\nu(s) \rangle = \sigma^2 \delta_{\gamma\nu} \delta_{ij} \delta(t - s)$.

In this case, we design the structures of two networks to be the same, i.e., $K_{ij}^A = K_{ij}^B$. The intensity of the internal coupling, $K_{ij}^A (= K_{ij}^B)$, is randomly and independently drawn from a uniform distribution $[-0.6, 0.6]$. Note that we choose the parameters so that each network can exhibit the collective oscillation which is a unique stable solution. Figure 2(b) shows the waveforms of all elements in network A for one period. Network B has similar waveforms as network A , but their periods of the limit-cycle solutions are slightly different. The frequencies of the collective oscillations of the two networks are $\Omega_A \simeq 0.159$ and $\Omega_B \simeq 0.148$ when there are no perturbations to the two networks.

The connection between two elements belonging to different networks is given as follows:

$$C_{ij}^{AB} = \begin{cases} 1 & \text{for } (i, j) = (9, 2), \\ 0 & \text{otherwise,} \end{cases} \quad (12)$$

$$C_{ij}^{BA} = \begin{cases} 1 & \text{for } (i, j) = (4, 2), \\ 0 & \text{otherwise.} \end{cases} \quad (13)$$

Figure 2(a) shows the schematic diagram of the connection between the two networks. The intensity of the external couplings is $\epsilon = 0.01$ and so weak that the collective oscillation of each network persists.

To apply the Bayesian inference, we generate a phase sampling data, $\{\Phi(t)\}$, from a time-series of an observed variable, which is chosen only one for each network. We choose v_5^A or $\sum_i v_i^A$ for network A , and v_5^B, v_8^B , or $\sum_i v_i^B$ for network B as the observed variables. The 5th element is excitable, and the 8th element is oscillatory. We record the times T_k^γ when the network γ intersects the Poincaré section at the k th time. The Poincaré section is set for each observed variable. In this case, we select $v_5^A = 0.0$ or $\sum_i v_i^A = 5.0$ for network A , and $v_5^B = 0.0, v_8^B = 0.0$, or $\sum_i v_i^B = 5.0$ for network B . These sections are chosen so that the trajectory of each network can intersect only once for one period.

To obtain $\{\Phi(t)\}$ using the train of T_k^γ , we interpolate the phase $\Phi_\gamma(t_l) \in [0, 2\pi)$ at time $t_l = l\Delta t$ ($l = 0, 1, \dots, L$). The value of phase $\Phi_\gamma(t_l)$, where t_l is between T_k^γ and T_{k+1}^γ , is obtained as follows:

$$\Phi_\gamma(t_l) = 2\pi \frac{t_l - T_k^\gamma}{T_{k+1}^\gamma - T_k^\gamma} \quad (T_k^\gamma \leq t_l < T_{k+1}^\gamma), \quad (14)$$

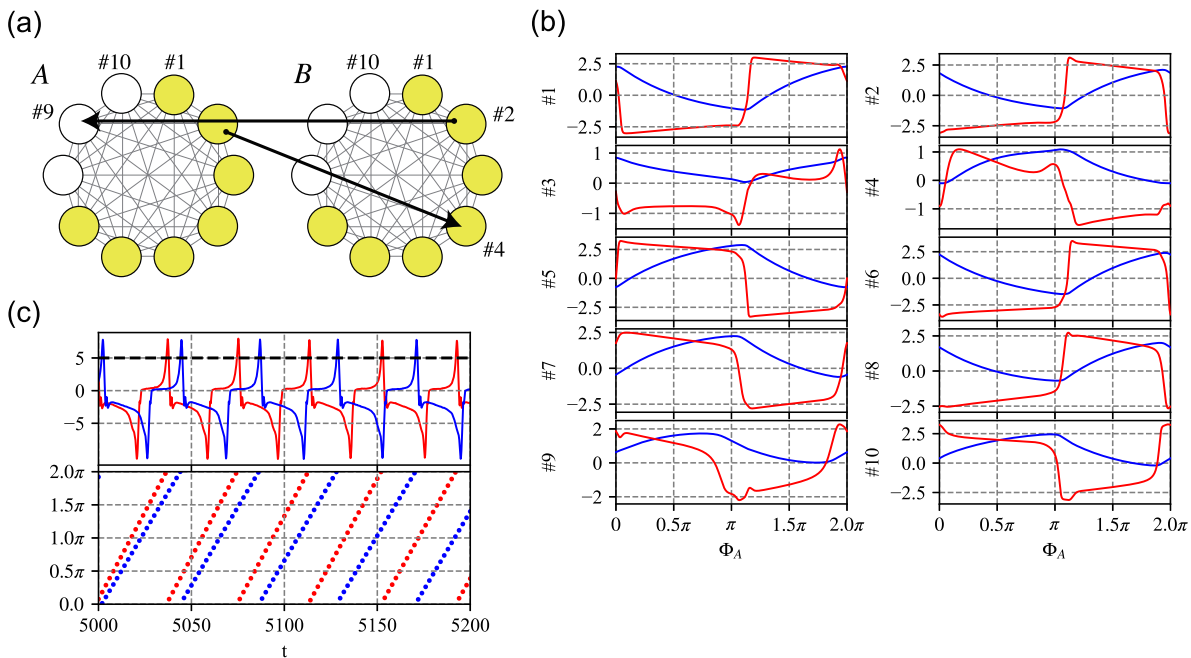


FIG. 2. Property of the dynamical system in Case 1. **(a)** Schematic diagram of networks A and B , each of which has 7 excitable elements (yellow circles) and 3 oscillatory elements (white circles). An arrow indicates an external coupling between two networks, corresponding to Eqs. (12) and (13). **(b)** Waveforms of network A . Each panel shows u_i^A (blue) and v_i^A (red) of elements i ($i = 1, 2, \dots, 10$) for one period as a function of Φ_A . Network B possesses similar trajectory due to $K_{ij}^A = K_{ij}^B$. **(c)** Time-series of the observed variables and phase variables. The time-series of $\sum_i v_i^A(t)$ (red) and $\sum_i v_i^B(t)$ (blue) are displayed in the upper panel. The Poincaré section (black dashed line) is fixed at $\sum_i v_i^A = 5.0$ for network A and $\sum_i v_i^B = 5.0$ for network B . The time-series of $\Phi_A(t)$ (red) and $\Phi_B(t)$ (blue) are displayed in the lower panel. The value of the phase is zero when the trajectory of each mean field intersects the Poincaré section. The intensity of the noise, $\eta_i^\gamma(t)$, is set to $\sigma = 0.01$.

where T_k^γ satisfies $\Phi_\gamma(T_k^\gamma) = 0$. The sampling interval is $\Delta t = 2.0$. Figure 2(c) shows the phase time-series of networks A and B generated from the time-series of $\sum_i v_i^A$ and $\sum_i v_i^B$.

We first confirm whether our method succeeds or not, and then investigate how the choice of observed variables affects the result of our method. Here, the hyperparameters in Eq. (7) are set to $\alpha_0 = \beta_0 = \lambda_0 = 1.0 \times 10^{-3}$, and the noise intensity is $\sigma = 0.01$. Figure 3(a) shows the phase equations of networks A and B estimated from the time-series of v_5^A and v_5^B . The length of the time-series satisfies $0 \leq |\Delta\Phi_{AB}(t)| \leq 200\pi$ ($t \simeq 5.5 \times 10^4$). The estimated phase equations are similar to the result obtained from the numerical method [59]. Figure 3(b) shows that the estimated model shown in Fig. 3(a) reproduced the distribution $P(\Delta\Phi_{BA})$ calculated from the phase time-series up to $t = 5.0 \times 10^5$.

Note that the phase value shifts when the observed variable changes, because the time to intersect the Poincaré section also varies depending on the trajectory of the observed variable. Figure 3(c) indicates that the time corresponding to $\Phi_A(t) = 0$ varies depending on the observed variable. The $\hat{\Gamma}_{AB}$ and $\hat{\Gamma}_{BA}$ also shift depending on the phase shift, as shown in Fig. 3(d), where the phase equations estimated from the time-series of v_5^A and v_8^B , instead of v_5^A and v_5^B , are plotted. In this study, the

phase shift is subtracted from the estimated model.

We calculate the prediction error of 100 trials for each set of observed variables to investigate the effect of the choice of observed variables on our method. The prediction error is calculated by comparing between the two phase equations, one of which is obtained using our Bayesian method and the other is calculated from the numerical method [59]. Figure 4(a) shows the comparison of the mean error pertaining to the phase equation of network A between the sets of observed variables (v_5^A, v_5^B) , $(v_5^A, \sum_i v_i^B)$, $(\sum_i v_i^A, v_5^B)$, $(\sum_i v_i^A, \sum_i v_i^B)$, and (v_5^A, v_8^B) , with the noise intensity, $\sigma = 0.01$. The observed variables have several properties: v_5^A and v_5^B are observed from one of the excitable elements in networks A and B , respectively; v_8^B is observed from one of the oscillatory elements in network B ; and $\sum_i v_i^A$ and $\sum_i v_i^B$ are the mean-field of all the elements in networks A and B , respectively. Each mean-field includes both excitable and oscillatory elements. The horizontal axis value, n , represents the length of phase time-series, e.g., $0 \leq |\Delta\Phi_{AB}(t)| \leq 2n\pi$. When the value of $|\Delta\Phi_{AB}(t)|$ increases by 2π , the phase time-series covers all of the state space of $\hat{\Gamma}_{AB}(\Delta\Phi_{AB})$. The vertical axis value represents the error value, which is calculated by integrating the difference between the estimated phase equation and the numerically calculated one. This value is normalized by

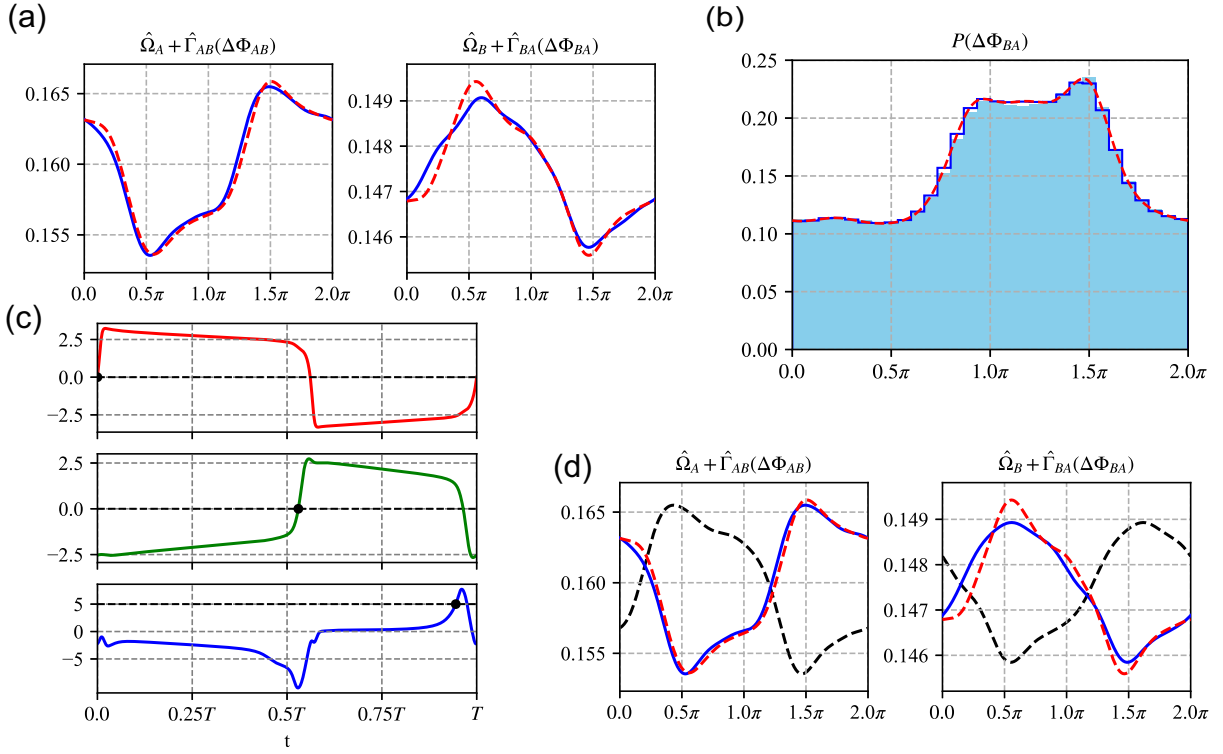


FIG. 3. A representative result of our method in Case 1. (a) Phase equations of networks A (left) and B (right) estimated from the time-series of v_5^A and v_5^B . The length of the time-series satisfies $0 \leq |\Delta\Phi_{AB}(t)| \leq 200\pi$ ($t \simeq 5.5 \times 10^4$). The blue solid curves are estimated using the Bayesian approach, whereas the red dashed curves are calculated using the numerical method [59]. (b) Distribution $P(\Delta\Phi_{BA})$ calculated from time-series (cyan) and the distribution reproduced from the estimated model (blue). Each distribution is obtained from the time-series up to $t = 5.0 \times 10^5$. The distribution analytically calculated from the true value of $\hat{\Gamma}_{AB}(-\Delta\Phi_{BA}) - \hat{\Gamma}_{BA}(\Delta\Phi_{BA})$ is also plotted (red). (c) Waveforms of $v_5^A(t)$ (top), $v_5^B(t)$ (middle), and $\sum_i v_i^A(t)$ (bottom) for one period on the limit-cycle orbit. The Poincaré sections set for each variable are also plotted (black dashed line). The phase shift results from the difference in the intersection time. (d) Phase equations of networks A (left) and B (right) estimated from the time-series of v_5^A and v_5^B . The red dashed curves are the same as those presented in panel (a). The black dashed curves are estimated using the Bayesian approach, and the blue solid curves are obtained by subtracting the phase shift from the originally estimated curves.

the amplitude of $\hat{\Gamma}_{AB}$, that is, the value of error is divided by $\pi(\max_{\Delta\Phi} \hat{\Gamma}_{AB}(\Delta\Phi) - \min_{\Delta\Phi} \hat{\Gamma}_{AB}(\Delta\Phi))$. We can find that the error decreases with an increase in the number of data points, and this decreasing trend is similar regardless of the types of observed variables. Figure 4(b) shows two estimated phase equations of network A ; one is for the set of observed variables (v_5^A, v_5^B) and the other is for $(\sum_i v_i^A, v_5^B)$. The length of the time-series satisfies $0 \leq |\Delta\Phi_{AB}(t)| \leq 200\pi$. The two curves are similar, and this fact is consistent with the results shown in Fig. 4(a). Figures 4(a) and 4(b) indicate that similar phase coupling functions are extracted by our method regardless of the types of observed variables. Figure 4(c) shows the mean and standard deviation calculated from 100 trials with the noise intensity $\sigma = 0.01, 0.02, 0.04$ for the set of observed variables (v_5^A, v_5^B). Although the standard deviation of error increases with σ becomes large, the convergence property is maintained as long as the noise is so weak that the collective oscillation persists.

B. Case 2: Three networks of FHN elements

We also investigated a case of three ($N = 3$) FHN networks. Figure 5(a) shows the schematic diagram of the three networks. This case is a generalization of Case 1 in terms of the number of networks and the network structure. The dynamics of element i ($i = 1, 2, \dots, 10$) in network $\gamma \in \{A, B, C\}$ is described as follows:

$$\begin{aligned} \dot{u}_i^\gamma &= \delta^\gamma (a + v_i^\gamma - bu_i^\gamma), \\ \dot{v}_i^\gamma &= v_i^\gamma - \frac{(v_i^\gamma)^3}{3} - u_i^\gamma + I_i + \sum_{j \neq i}^{10} K_{ij}^\gamma (v_j^\gamma - v_i^\gamma) \\ &\quad + \epsilon \sum_{\nu \neq \gamma} \sum_{j=1}^{10} C_{ij}^{\gamma\nu} (v_j^\nu - v_i^\gamma) + \eta_i^\gamma(t), \end{aligned} \quad (15)$$

$$(16)$$

where $\nu \in \{A, B, C\}$ is also index of networks, which is different from γ , i.e., $\nu \neq \gamma$. The values of I_i , a , and b are the same as those in Sec. III A. The time constants

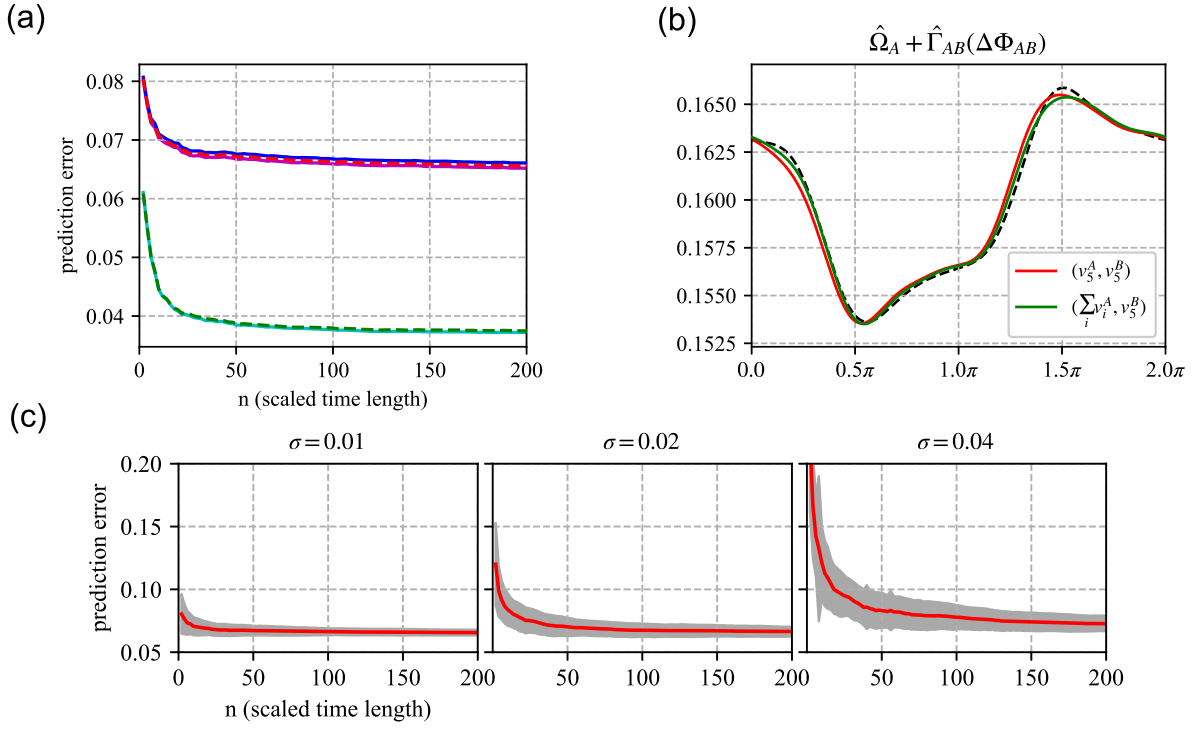


FIG. 4. Statistics of the prediction error calculated from 100 trials in Case 1. **(a)** Mean of the prediction error pertaining to the phase equation of network A calculated from 100 trials. The intensity of noise is $\sigma = 0.01$. The length of the time-series satisfies $0 \leq |\Delta\Phi_{AB}(t)| \leq 2n\pi$, where n is the horizontal axis value. The error (vertical axis) is calculated by integrating the difference between two curves (e.g., the red dashed curve and blue solid curve shown in Fig. 3(a)) from 0 to 2π and then divided by true value of $\pi(\max_{\Delta\Phi} \hat{\Gamma}_{AB}(\Delta\Phi) - \min_{\Delta\Phi} \hat{\Gamma}_{AB}(\Delta\Phi))$. The sets of observed variables are (v_5^A, v_5^B) (red), $(v_5^A, \sum_i v_i^B)$ (blue), $(\sum_i v_i^A, v_5^B)$ (green), $(\sum_i v_i^A, \sum_i v_i^B)$ (cyan), and (v_5^A, v_8^B) (magenta). **(b)** Phase equations of network A estimated from a time-series. The length of the time-series satisfies $0 \leq |\Delta\Phi_{AB}(t)| \leq 200\pi$. The sets of observed variables are (v_5^A, v_5^B) (red) and $(\sum_i v_i^A, v_5^B)$ (green). The black dashed curve is the result of the numerical method [59]. **(c)** Mean (red curve) and standard deviation (gray) of prediction error calculated from 100 trials. The set of observed variables is (v_5^A, v_5^B) . The intensity of noise is $\sigma = 0.01$ (left), 0.02 (middle), and 0.04 (right).

are set to $\delta^A = 0.080$, $\delta^B = 0.096$, and $\delta^C = 0.086$. The intensity of noise is set to $\sigma = 0.005$.

We design each network structure to be different, i.e., $K_{ij}^A \neq K_{ij}^B \neq K_{ij}^C$, each of which is randomly and independently drawn from a uniform distribution $[-0.6, 0.6]$. The waveforms of the limit-cycle solution of each network are different, mainly due to the differences in network structures (Fig. 8 in Appendix A). Figure 5(a) shows that the connection between networks is given by

$$\begin{cases} C_{9\ 2}^{AB} = C_{6\ 2}^{BA} = C_{10\ 2}^{CA} = C_{7\ 2}^{BC} = C_{5\ 2}^{CB} = 1, \\ C_{ij}^{\gamma\nu} = 0 \text{ otherwise,} \end{cases} \quad (17)$$

where there are no couplings from network C to network A , thus, the phase coupling function, $\hat{\Gamma}_{AC}$, should be zero. The intensity of the external couplings is set to $\epsilon = 0.01$.

In this case, we choose $\sum_i v_i^A$ for network A , v_5^B or $\sum_i v_i^B$ for network B , and v_5^C, v_8^C , or $\sum_i v_i^C$ for network C as the observed variables. The Poincaré section is set to $\sum_i v_i^A = 0.0$ for network A , $v_5^B = 0.0$ or $\sum_i v_i^B = -5.0$ for network B , and $v_5^C = 0.0, v_8^C = 0.0$, or $\sum_i v_i^C = 2.0$

for network C . The hyperparameters in Eq. (7) are set to $\alpha_0 = \beta_0 = \lambda_0 = 1.0 \times 10^{-2}$.

Figure 5(b) is a representative result of our method. This result is obtained from the time-series of $\sum_i v_i^A$, $\sum_i v_i^B$, and $\sum_i v_i^C$, which satisfy $0 \leq |\Delta\Phi_{AB}(t)| \leq 200\pi$ ($t \simeq 9.4 \times 10^4$). Figure 5(c) indicates that the estimated model shown in Fig. 5(b) can reproduce similar distributions $P(\Delta\Phi_{AB})$, $P(\Delta\Phi_{AC})$, and $P(\Delta\Phi_{BC})$, which are calculated from the time-series up to $t = 5.0 \times 10^5$.

Further, we also investigated the prediction error for each observed variable in the same way as Sec. III A. Figure 6(a) shows the mean value of the prediction error pertaining to the phase coupling function, $\hat{\Gamma}_{BC}$, calculated from 100 trials, and the values of error are similar regardless of the observed variables. Figure 6(b) shows the two estimations of $\hat{\Gamma}_{BC}$; one is for the set of observed variables $(\sum_i v_i^A, v_5^B, v_5^C)$ and the other is for $(\sum_i v_i^A, \sum_i v_i^B, v_5^C)$, and these two curves are similar. Figures 6(c) and 6(d) show the results for $\hat{\Gamma}_{CA}$ in the same way as Figs. 6(a) and 6(b).

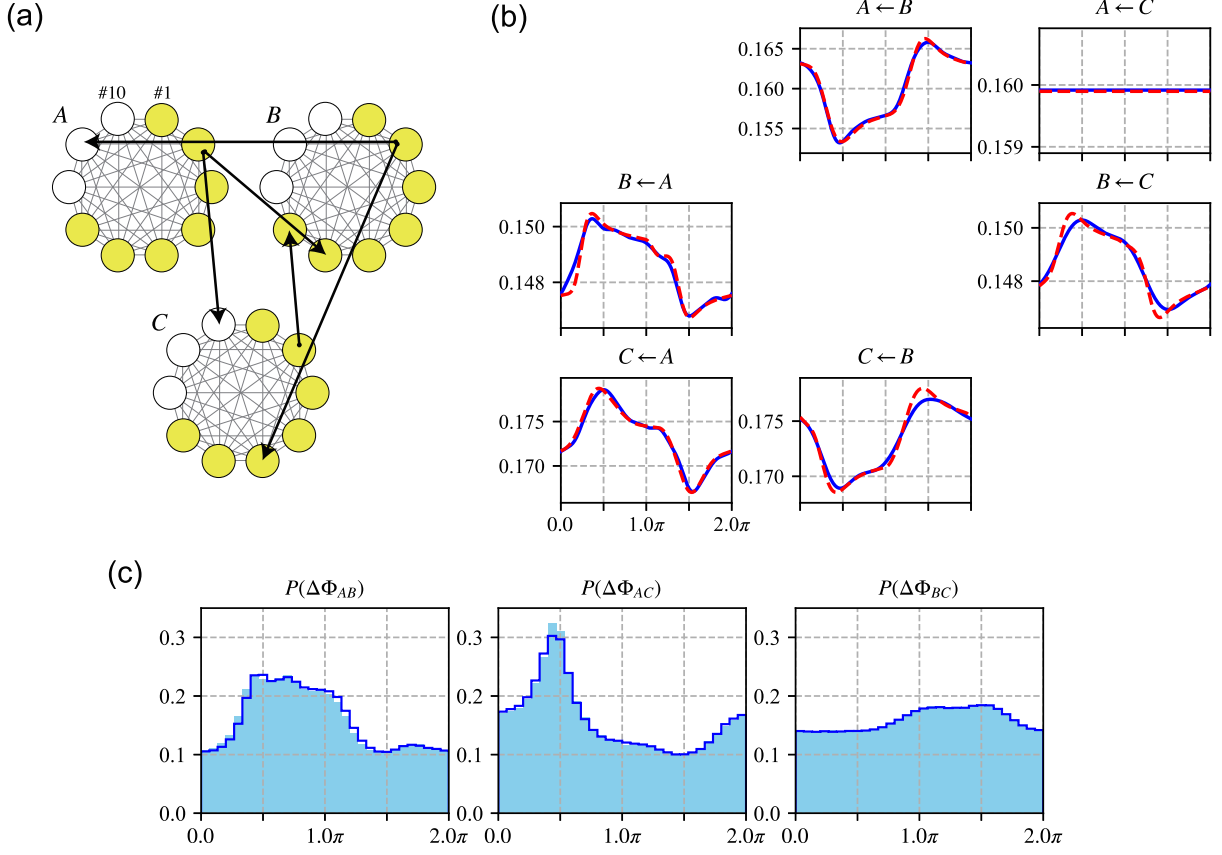


FIG. 5. Property of the dynamical system and a representative result of the model identification in Case 2. **(a)** Schematic diagram of networks A , B , and C , each of which has 7 excitable elements (yellow circles) and 3 oscillatory elements (white circles). An arrow indicates an external coupling between networks, which corresponds to Eq. (17). **(b)** Phase coupling functions with constant term, $\hat{\Omega}_\gamma$, estimated from the time-series of $\sum_i v_i^A$, $\sum_i v_i^B$, and $\sum_i v_i^C$. The length of the time-series satisfies $0 \leq |\Delta\Phi_{AB}(t)| \leq 200\pi$ ($t \simeq 9.4 \times 10^4$). The blue solid curves are estimated using the Bayesian approach, whereas the red dashed curves are calculated using the numerical method. The sender and receiver indexes of the coupling functions are shown at the top of each panel. **(c)** Distributions $P(\Delta\Phi_{AB})$ (left), $P(\Delta\Phi_{AC})$ (middle), and $P(\Delta\Phi_{BC})$ (right) calculated from time-series (cyan) and the distributions reproduced using the estimated model (blue). Each distribution is obtained from the time-series up to $t = 5.0 \times 10^5$.

C. Case 3: Two networks of van der Pol oscillators follows

We also investigated a case of two ($N = 2$) van der Pol networks. Figure 7(a) shows the schematic diagram of the two networks. In this case, we employ another type of element that oscillates slowly (not a fast-slow system such as the FHN element), and apply the Hilbert transform [12] to transform observed time-series into phase time-series, instead of linear interpolation described in Eq. (14). The linear interpolation method averages the effect of perturbations to a network on the phase variable for one period, whereas the Hilbert transform reflects perturbations in phase time-series without averaging.

The state variables of each element in network γ is represented by $\mathbf{X}_i^\gamma = (u_i^\gamma, v_i^\gamma)$ ($i = 1, 2, \dots, 10$), which

$$\begin{aligned} \dot{u}_i^\gamma &= v_i^\gamma, \\ \dot{v}_i^\gamma &= -u_i^\gamma - a^\gamma v_i^\gamma ((u_i^\gamma)^2 - 1) + \sum_{j \neq i}^{10} K_{ij}^\gamma (v_j^\gamma - v_i^\gamma) \\ &\quad + \epsilon \sum_{j=1}^{10} C_{ij}^{\gamma\nu} ((v_j^\nu)^2 u_i^\gamma - (v_i^\nu)^2 u_j^\nu) + \eta_i^\gamma(t), \end{aligned} \quad (18)$$

where $(\gamma, \nu) = (A, B), (B, A)$. The nonlinearity parameters are set to $a^A = 0.5$ and $a^B = 0.3$, and the noise intensity is $\sigma = 0.005$. The structures of two networks are designed to be different, i.e., $K_{ij}^A \neq K_{ij}^B$, each of which is randomly and independently drawn from a uniform distribution $[-0.6, 0.6]$. We choose these parameters so that each network can exhibit the collective oscillation (Fig. 9 in Appendix A). Figure 7(a) show that the connection

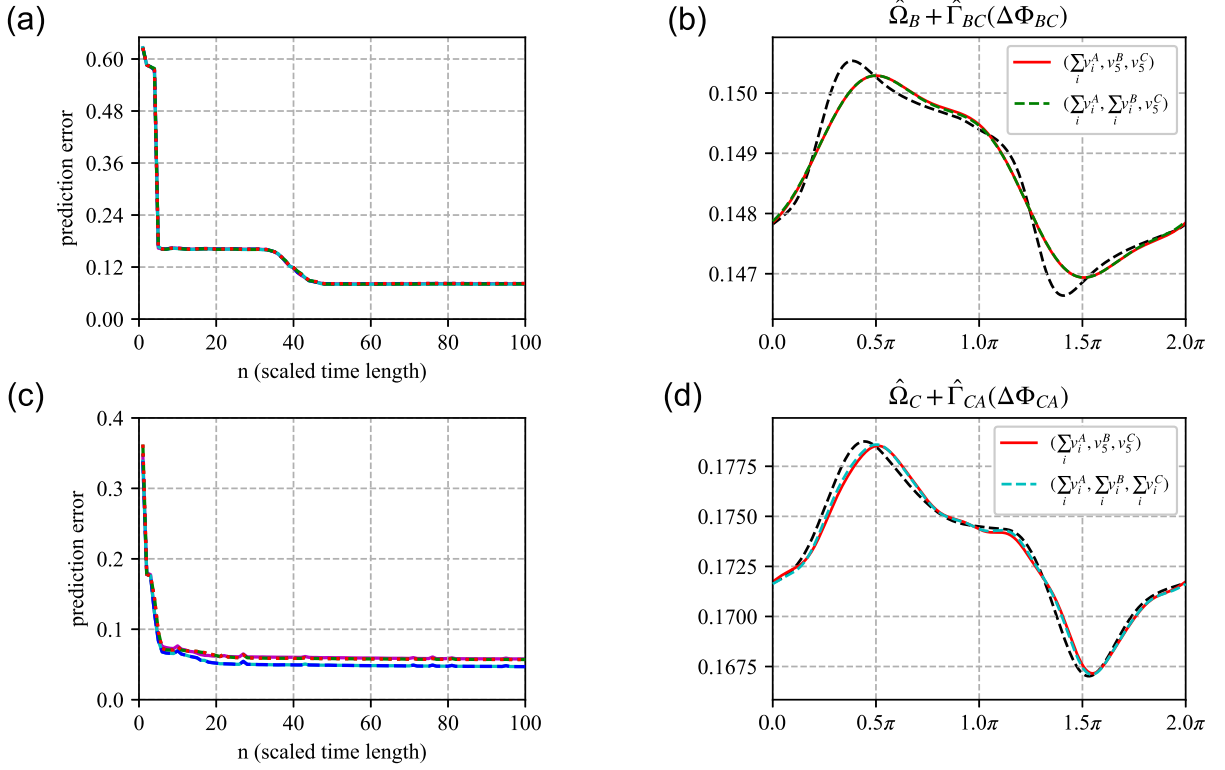


FIG. 6. Statistics of the prediction error calculated from 100 trials in Case 2. **(a)** Mean of the prediction error pertaining to the phase coupling function, $\hat{\Gamma}_{BC}(\Delta\Phi_{BC})$, calculated from 100 trials. The length of the time-series satisfies $0 \leq |\Delta\Phi_{BC}(t)| \leq 2n\pi$, where n is the horizontal axis value. The value of error (vertical axis) is divided by $\pi(\max_{\Delta\Phi} \hat{\Gamma}_{BC}(\Delta\Phi) - \min_{\Delta\Phi} \hat{\Gamma}_{BC}(\Delta\Phi))$. The sets of observed variables are $(\sum_i v_i^A, v_5^B, v_5^C)$ (red), $(\sum_i v_i^A, v_5^B, \sum_i v_i^C)$ (blue), $(\sum_i v_i^A, \sum_i v_i^B, v_5^C)$ (green), $(\sum_i v_i^A, \sum_i v_i^B, \sum_i v_i^C)$ (cyan), and $(\sum_i v_i^A, v_5^B, v_5^C)$ (magenta). These five curves have a similar shape to each other. **(b)** Phase coupling functions $\hat{\Gamma}_{BC}(\Delta\Phi_{BC})$ estimated from a time-series. The length of the time-series satisfies $0 \leq |\Delta\Phi_{AB}(t)| \leq 200\pi$. The sets of observed variables are $(\sum_i v_i^A, v_5^B, v_5^C)$ (red) and $(\sum_i v_i^A, \sum_i v_i^B, v_5^C)$ (green). The black dashed curve is the result of the numerical method. **(c)** & **(d)** Results for $\hat{\Gamma}_{CA}(\Delta\Phi_{CA})$ are shown in the same way as panels (a) and (b).

between two networks is given as follows:

$$C_{ij}^{AB} = \begin{cases} 1 & \text{for } (i, j) = (1, 2), (10, 3), \\ 0 & \text{otherwise,} \end{cases} \quad (20)$$

$$C_{ij}^{BA} = \begin{cases} 1 & \text{for } (i, j) = (2, 2), (3, 3), \\ 0 & \text{otherwise.} \end{cases} \quad (21)$$

The intensity of the external couplings is set to $\epsilon = 0.005$.

We observe the time-series of v_5^A or v_{10}^A from network A , and v_2^B or v_{10}^B from network B . Each time-series is observed from one of the oscillators. We denote the dynamics observed from network γ at time t as $s_\gamma(t)$ for simplicity. To transform $s_\gamma(t)$ into phase time-series $\Theta_\gamma(t)$, we use Hilbert transformation $s^{\mathcal{H}}(t)$ as follows [12]:

$$A_\gamma(t)e^{i\Theta_\gamma(t)} = s_\gamma(t) + is_\gamma^{\mathcal{H}}(t), \quad (22)$$

where $A_\gamma(t)$ is the amplitude of the equation's right-hand side. Note that the phase $\Theta_\gamma(t)$ does not increase linearly with time even in the absence of perturbations to the network γ . This property comes from the nonlinearity of

the dynamics. Therefore, we construct a new phase time-series, $\Phi_\gamma(t)$, from the existing one, Θ_γ , as follows [17, 18, 20]:

$$\Phi_\gamma(\Theta_\gamma) = 2\pi \int_0^{\Theta_\gamma} f_\gamma(\Theta') d\Theta', \quad (23)$$

where $f_\gamma(\Theta_\gamma)$ is the probability density function of Θ_γ . Figure 7(b) shows the time-series of v_5^A , v_2^B , Φ_A , and Φ_B , where each phase increases linearly with time.

Figure 7(c) shows the dynamics of networks A and B estimated from the time-series of v_5^A and v_2^B . The hyperparameters in Eq. (7) are set to $\alpha_0 = \beta_0 = \lambda_0 = 1.0 \times 10^{-3}$, and the length of the time-series used for the model identification satisfies $0 \leq |\Delta\Phi_{AB}(t)| \leq 200\pi$.

We investigated the effect of the choice of observed variables in the same way as Secs. III A and III B. Figure 7(d) shows the mean of the prediction error pertaining to the phase equation for network A . Figure 7(e) shows the estimated phase equation for network A for each set of observed variables. Figures 7(f) and 7(g) show

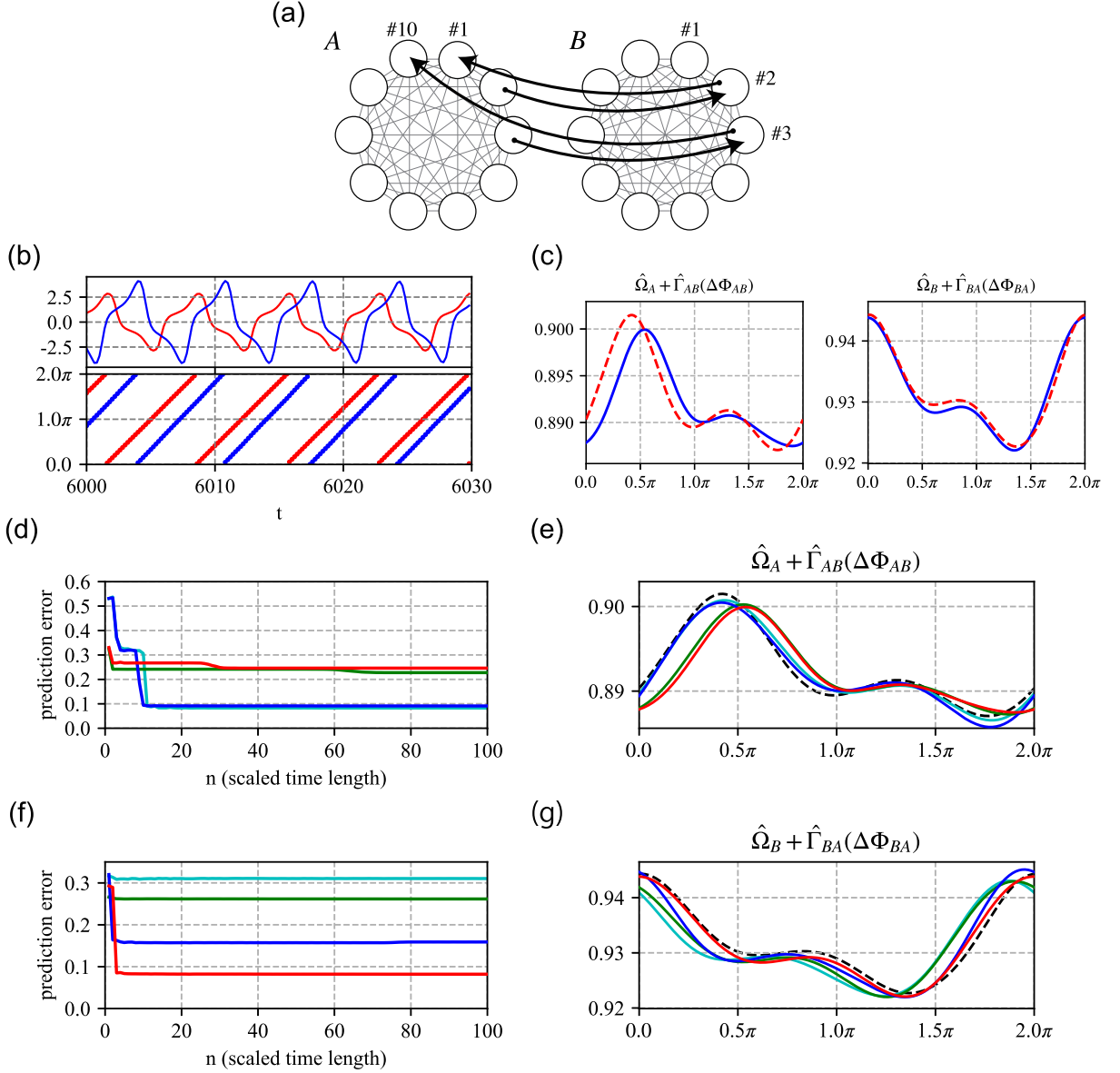


FIG. 7. Property of the dynamical system and overall result of the model identification in Case 3. **(a)** Schematic diagram of networks A and B , each of which has 10 oscillatory elements (white circles). An arrow indicates an external coupling between two networks, corresponding to Eqs. (20) and (21). **(b)** Time-series of the observed variables and phase variables. The time-series of v_5^A (red) and v_2^B (blue) are shown in the upper panel, and those of Φ_A (red) and Φ_B (blue) are shown in the lower panel. The sampling interval is set to $\Delta t = 0.2$. **(c)** Phase equations of networks A (left) and B (right) estimated from the time-series of v_5^A and v_2^B . The length of the time-series satisfies $0 \leq |\Delta\Phi_{AB}(t)| \leq 200\pi$. The blue solid curves are estimated using the Bayesian approach, whereas the red dashed curves are calculated using the numerical method. **(d)** Mean of the prediction error pertaining to the phase equation of network A calculated from 100 trials. The length of the time-series satisfies $0 \leq |\Delta\Phi_{AB}(t)| \leq 2n\pi$, where n is the value of the horizontal axis. The value of error (vertical axis) is divided by the true value of $\pi(\max_{\Delta\Phi} \hat{\Gamma}_{AB}(\Delta\Phi) - \min_{\Delta\Phi} \hat{\Gamma}_{AB}(\Delta\Phi))$. The sets of observed variables are (v_5^A, v_2^B) (red), (v_{10}^A, v_2^B) (blue), (v_5^A, v_{10}^B) (green), and (v_{10}^A, v_{10}^B) (cyan). **(e)** Phase equations of network A estimated from each set of observed variables. The length of the time-series satisfies $0 \leq |\Delta\Phi_{AB}(t)| \leq 200\pi$. The colors of curves and the sets of observed variables are the same as those in panel (d). The black dashed curve is the result of the numerical method. **(f)** & **(g)** Results for network B are shown in the same way as panels (d) and (e).

the results for network B in the same way as Figs. 7(d) and 7(e).

IV. DISCUSSION

We extended the range of applications of the Bayesian inference method [31] from a phase representing the state of an oscillator to a macroscopic phase representing the state of an entire network exhibiting collective oscillation [59], and demonstrated the Bayesian method in the three cases (Secs. III A, III B, and III C) to extract macroscopic phase coupling functions, which describe the synchronization mechanism between networks, directly from time-series data. In Sec. III A, we considered the case of two networks of FHN elements, which have both excitable and oscillatory elements. In Sec. III B, we considered the case of three networks of FHN elements as a generalization of Sec. III A in terms of the number of networks and the structures of internal couplings. In Sec. III C, we investigated the case of two networks of van der Pol oscillators. In those cases, we considered the three types of observed variables: one excitable element, one oscillatory element, and mean-field, to evaluate how the choice of the observed variables affects the statistical inference for the phase coupling functions.

Our results show that the same phase coupling function can be extracted from the time-series of any one element in each network as well as from the time-series of each network's mean-field. These results indicate that the statistical inference for phase coupling function is not affected by the choice of the observed variables, thus, we can consistently extract the macroscopic phase coupling function between networks. In addition, we extracted the macroscopic phase coupling function between networks consistently regardless of the two transformation methods from observed time-series to phase time-series, i.e., linear interpolation for networks of FHN elements (Secs. III A and III B) and the Hilbert transform for networks of van der Pol oscillators (Sec. III C). We should remark that the assumption of collective oscillation enables us to extract the macroscopic phase coupling function from the time-series of an excitable element, although the conventional phase reduction theory cannot apply to an excitable element. The ability to extract the macroscopic coupling function regardless of the transformation method to phase time-series and the types of observed variables is useful in experimental situations.

In this study, we considered the macroscopic phase description where each network exhibits collective oscillation as described in Ref. [59]. This phase description has been generalized to the rhythmic spatiotemporal

dynamics such as reaction-diffusion systems [60]. Further, some other theoretical frameworks for a network's phase response analysis have been developed: phase coherent states in globally coupled noisy identical oscillators [52, 53, 55], partially phase-locked states in globally coupled noiseless nonidentical oscillators [56], and fully phase-locked states in networks of coupled nonidentical elements [57, 58]. Particularly, the framework developed in Ref. [54] is a generalization for a network of globally coupled noisy identical oscillators to address excitable elements and strong internal couplings. This type of generalization corresponds to the assumption we employed in this study. We will attempt to extend the range of application of the Bayesian inference method [31] for the aforementioned situations in future research.

Combining the Bayesian inference and the concept of collective oscillation may provide a significant insight into the analysis of the macroscopic coupling function between networks. As mentioned in Sec. I, there are various ways to observe the dynamics of brain regions for analyzing coupling functions between them. Our results suggest that we can extract the macroscopic phase coupling function regardless of either from the time-series of each LFP or from any one neuron's spike in each region if neural populations in brain regions exhibit collective oscillations. Arguably, the Bayesian method used in this study can apply to various domains because this method only assumes that each network exhibits collective oscillation, where all elements in a network oscillate with the same period.

ACKNOWLEDGMENTS

This work was supported by JSPS (Japan) KAKENHI Grant Numbers JP20K21810, JP20K20520, JP20H04144, JP20K03797, JP18H03205, JP17H03279.

Appendix A: Supplemental information for Case 2 and Case 3

Figure 8 shows the waveforms for one period of each network exhibiting collective oscillation in Case 2. The frequencies of the collective oscillations of the three networks are $\Omega_A \simeq 0.159$, $\Omega_B \simeq 0.148$, and $\Omega_C \simeq 0.172$.

Figure 9 shows the waveforms for one period of each network exhibiting collective oscillation in Case 3. The frequencies of the collective oscillations of the two networks are $\Omega_A \simeq 0.900$ and $\Omega_B \simeq 0.939$.

[1] Y. Kuramoto, *Chemical oscillations, waves, and turbulence* (Springer-Verlag, Berlin, 1984).

[2] S. H. Strogatz, From Kuramoto to Crawford: exploring the onset of synchronization in populations of coupled os-

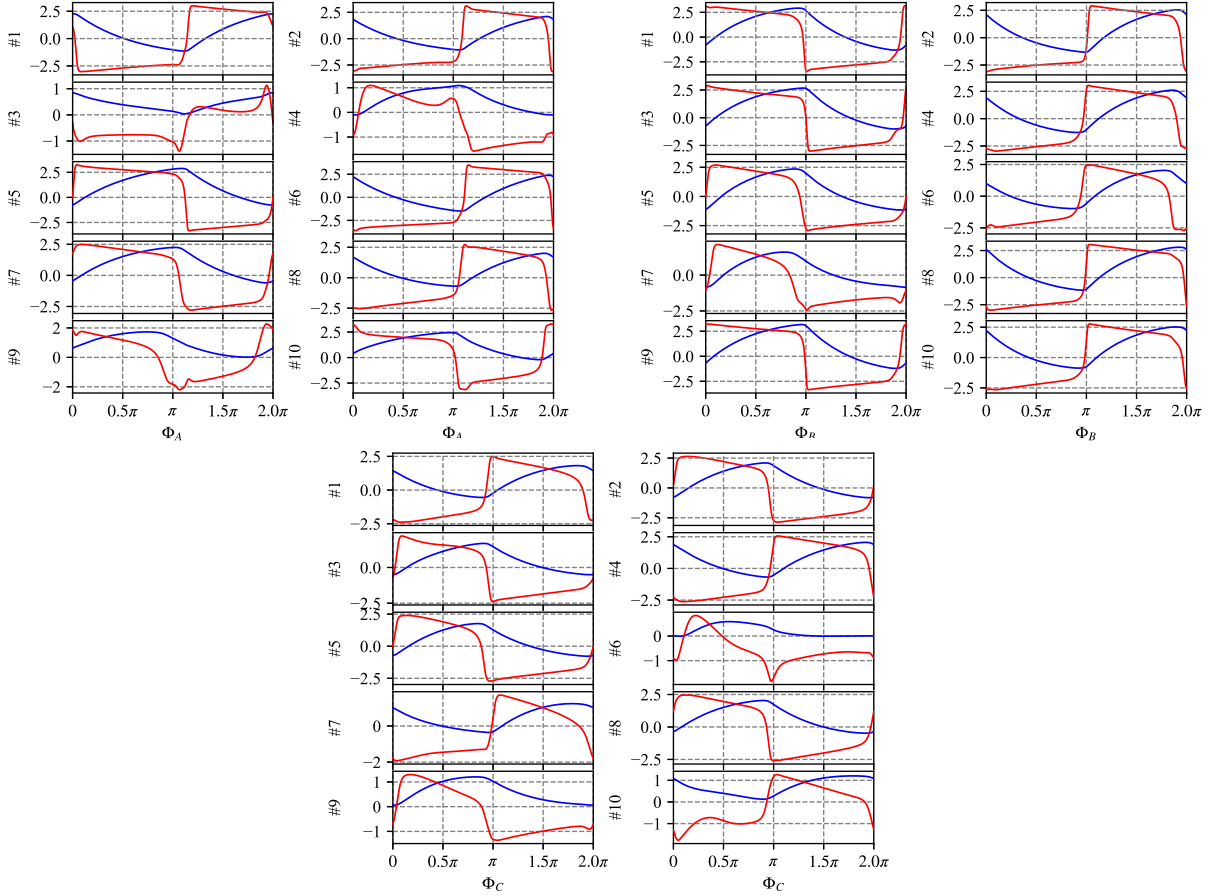


FIG. 8. Waveforms of networks A (top left), B (top right), and C (lower middle) exhibiting collective oscillations in Case 2. Each panel shows $u_i^\gamma(\Phi_\gamma)$ (blue) and $v_i^\gamma(\Phi_\gamma)$ (red) for one period of element i ($i = 1, 2, \dots, 10$) in network $\gamma \in \{A, B, C\}$.

- illators, *Physica D: Nonlinear Phenomena* **143**, 1 (2000).
- [3] J. A. Acebrón, L. L. Bonilla, C. J. Pérez Vicente, F. Ritort, and R. Spigler, The Kuramoto model: A simple paradigm for synchronization phenomena, *Reviews of Modern Physics* **77**, 137 (2005).
- [4] A. Arenas, A. Díaz-Guilera, J. Kurths, Y. Moreno, and C. Zhou, Synchronization in complex networks, *Physics Reports* **469**, 93 (2008).
- [5] S. N. Dorogovtsev, A. V. Goltsev, and J. F. F. Mendes, Critical phenomena in complex networks, *Reviews of Modern Physics* **80**, 1275 (2008).
- [6] A. T. Winfree, Biological rhythms and the behavior of populations of coupled oscillators, *Journal of Theoretical Biology* **16**, 15 (1967).
- [7] A. T. Winfree, *The geometry of biological time* (Springer, New York, 2001).
- [8] G. B. Ermentrout and N. Kopell, Multiple pulse interactions and averaging in systems of coupled neural oscillators, *Journal of Mathematical Biology* **29**, 195 (1991).
- [9] G. B. Ermentrout, Stable Periodic Solutions to Discrete and Continuum Arrays of Weakly Coupled Nonlinear Oscillators, *SIAM Journal on Applied Mathematics* **52**, 1665 (1992).
- [10] B. Ermentrout, Type I Membranes, Phase Resetting Curves, and Synchrony, *Neural Computation* **8**, 979 (1996).
- [11] A. Pikovsky and S. Ruffo, Finite-size effects in a population of interacting oscillators, *Physical Review E* **59**, 1633 (1999).
- [12] A. Pikovsky, M. Rosenblum, and J. Kurths, *Synchronization: A Universal Concept in Nonlinear Sciences* (Cambridge University Press, Cambridge, 2001).
- [13] E. Brown, J. Moehlis, and P. Holmes, On the Phase Reduction and Response Dynamics of Neural Oscillator Populations, *Neural Computation* **16**, 673 (2004).
- [14] E. M. Izhikevich, *Dynamical systems in neuroscience: the geometry of excitability and bursting* (MIT Press, Cambridge, Mass, 2007).
- [15] P. Ashwin, S. Coombes, and R. Nicks, Mathematical Frameworks for Oscillatory Network Dynamics in Neuroscience, *The Journal of Mathematical Neuroscience* **6**, 2 (2016).
- [16] H. Nakao, Phase reduction approach to synchronisation of nonlinear oscillators, *Contemporary Physics* **57**, 188 (2016).
- [17] B. Kralemann, L. Cimponeriu, M. Rosenblum, A. Pikovsky, and R. Mrowka, Uncovering interaction of coupled oscillators from data, *Physical Review E* **76**, 055201 (2007).
- [18] B. Kralemann, L. Cimponeriu, M. Rosenblum,

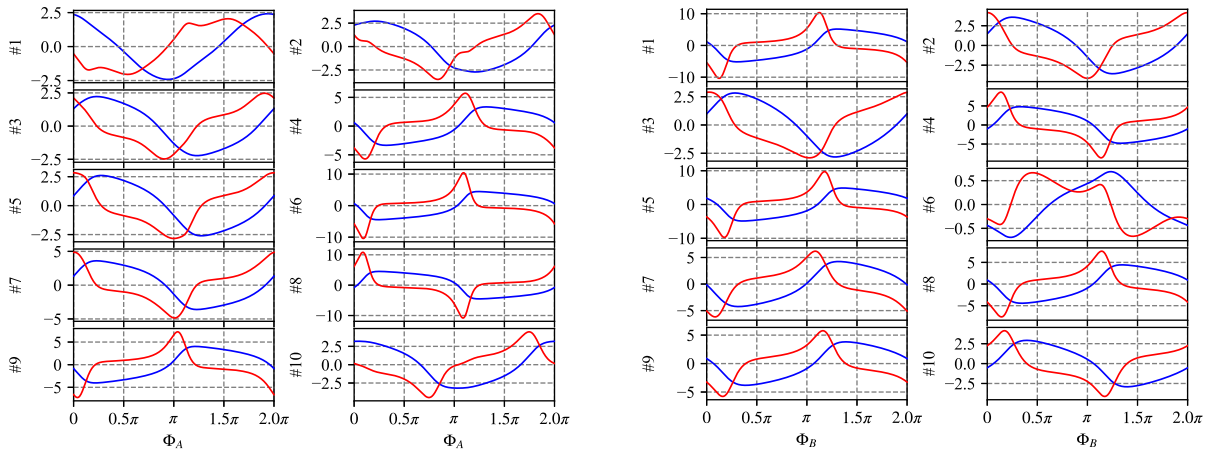


FIG. 9. Waveforms of networks A (left) and B (right) exhibiting collective oscillations in Case 3. Each panel shows $u_i^\gamma(\Phi_\gamma)$ (blue) and $v_i^\gamma(\Phi_\gamma)$ (red) for one period of element i ($i = 1, 2, \dots, 10$) in network $\gamma \in \{A, B\}$.

- A. Pikovsky, and R. Mrowka, Phase dynamics of coupled oscillators reconstructed from data, *Physical Review E* **77**, 066205 (2008).
- [19] B. Kralemann, A. Pikovsky, and M. Rosenblum, Reconstructing phase dynamics of oscillator networks, *Chaos: An Interdisciplinary Journal of Nonlinear Science* **21**, 025104 (2011).
- [20] B. Kralemann, A. Pikovsky, and M. Rosenblum, Reconstructing effective phase connectivity of oscillator networks from observations, *New Journal of Physics* , 085013 (2014).
- [21] B. Kralemann, M. Frühwirth, A. Pikovsky, M. Rosenblum, T. Kenner, J. Schaefer, and M. Moser, In vivo cardiac phase response curve elucidates human respiratory heart rate variability, *Nature Communications* **4**, 2418 (2013).
- [22] R. F. Galán, G. B. Ermentrout, and N. N. Urban, Efficient Estimation of Phase-Resetting Curves in Real Neurons and its Significance for Neural-Network Modeling, *Physical Review Letters* **94**, 158101 (2005).
- [23] G. B. Ermentrout, R. F. Galán, and N. N. Urban, Relating Neural Dynamics to Neural Coding, *Physical Review Letters* **99**, 248103 (2007).
- [24] K. Ota, M. Nomura, and T. Aoyagi, Weighted Spike-Triggered Average of a Fluctuating Stimulus Yielding the Phase Response Curve, *Phys. Rev. Lett.* **103**, 024101 (2009).
- [25] T. Imai and T. Aoyagi, Improvement effect of measuring phase response curves by using multicycle data, *Nonlinear Theory and Its Applications, IEICE* **7**, 58 (2016).
- [26] T. Funato, Y. Yamamoto, S. Aoi, T. Imai, T. Aoyagi, N. Tomita, and K. Tsuchiya, Evaluation of the Phase-Dependent Rhythm Control of Human Walking Using Phase Response Curves, *PLOS Computational Biology* **12**, 1 (2016).
- [27] C. M. Bishop, *Pattern recognition and machine learning* (Springer, New York, 2006).
- [28] T. Stankovski, A. Duggento, P. V. E. McClintock, and A. Stefanovska, Inference of Time-Evolving Coupled Dynamical Systems in the Presence of Noise, *Physical Review Letters* **109**, 024101 (2012).
- [29] T. Stankovski, Time-varying coupling functions: Dynamical inference and cause of synchronization transitions, *Physical Review E* **95**, 022206 (2017).
- [30] Z. Hagos, T. Stankovski, J. Newman, T. Pereira, P. V. E. McClintock, and A. Stefanovska, Synchronization transitions caused by time-varying coupling functions, *Philosophical Transactions of the Royal Society A: Mathematical, Physical and Engineering Sciences* **377**, 20190275 (2019).
- [31] K. Ota and T. Aoyagi, Direct extraction of phase dynamics from fluctuating rhythmic data based on a Bayesian approach, arXiv:1405.4126 (2014).
- [32] K. Ota, I. Aihara, and T. Aoyagi, Interaction mechanisms quantified from dynamical features of frog choruses, *Royal Society Open Science* **7**, 191693 (2020).
- [33] T. Stankovski, V. Ticcinielli, P. V. E. McClintock, and A. Stefanovska, Coupling functions in networks of oscillators, *New Journal of Physics* **17**, 035002 (2015).
- [34] T. Stankovski, S. Petkoski, J. Raeder, A. F. Smith, P. V. E. McClintock, and A. Stefanovska, Alterations in the coupling functions between cortical and cardio-respiratory oscillations due to anaesthesia with propofol and sevoflurane, *Philosophical Transactions of the Royal Society A: Mathematical, Physical and Engineering Sciences* **374**, 20150186 (2016).
- [35] T. Stankovski, V. Ticcinielli, P. V. E. McClintock, and A. Stefanovska, Neural Cross-Frequency Coupling Functions, *Frontiers in Systems Neuroscience* **11**, 33 (2017).
- [36] T. Onojima, T. Goto, H. Mizuhara, and T. Aoyagi, A dynamical systems approach for estimating phase interactions between rhythms of different frequencies from experimental data, *PLOS Computational Biology* **14**, e1005928 (2018).
- [37] K. Suzuki, T. Aoyagi, and K. Kitano, Bayesian Estimation of Phase Dynamics Based on Partially Sampled Spikes Generated by Realistic Model Neurons, *Frontiers in Computational Neuroscience* **11**, 116 (2018).
- [38] V. Sakkalis, Review of advanced techniques for the estimation of brain connectivity measured with EEG/MEG, *Computers in Biology and Medicine* **41**, 1110 (2011).
- [39] A. Jafarian, P. Zeidman, V. Litvak, and K. Friston,

- Structure learning in coupled dynamical systems and dynamic causal modelling, *Philosophical Transactions of the Royal Society A: Mathematical, Physical and Engineering Sciences* **377**, 20190048 (2019).
- [40] A. Ponce-Alvarez, G. Deco, P. Hagmann, G. L. Romani, D. Mantini, and M. Corbetta, Resting-State Temporal Synchronization Networks Emerge from Connectivity Topology and Heterogeneity, *PLOS Computational Biology* **11**, e1004100 (2015).
- [41] R. E. Rosch, P. R. Hunter, T. Baldeweg, K. J. Friston, and M. P. Meyer, Calcium imaging and dynamic causal modelling reveal brain-wide changes in effective connectivity and synaptic dynamics during epileptic seizures, *PLOS Computational Biology* **14**, e1006375 (2018).
- [42] P. van Mierlo, Y. Höller, N. K. Focke, and S. Vulliemoz, Network Perspectives on Epilepsy Using EEG/MEG Source Connectivity, *Frontiers in Neurology* **10**, 721 (2019).
- [43] H.-J. Park and K. Friston, Structural and Functional Brain Networks: From Connections to Cognition, *Science* **342**, 1238411 (2013).
- [44] T. Stankovski, Coupling Functions in Neuroscience, arXiv:2008.07612 (2020).
- [45] A. Pikovsky and M. Rosenblum, Dynamics of globally coupled oscillators: Progress and perspectives, *Chaos: An Interdisciplinary Journal of Nonlinear Science* **25**, 097616 (2015).
- [46] A. Pikovsky and M. Rosenblum, Partially Integrable Dynamics of Hierarchical Populations of Coupled Oscillators, *Physical Review Letters* **101**, 264103 (2008).
- [47] A. Pikovsky and M. Rosenblum, Dynamics of heterogeneous oscillator ensembles in terms of collective variables, *Physica D: Nonlinear Phenomena* **240**, 872 (2011).
- [48] S. Watanabe and S. H. Strogatz, Integrability of a globally coupled oscillator array, *Physical Review Letters* **70**, 2391 (1993).
- [49] S. Watanabe and S. H. Strogatz, Constants of motion for superconducting Josephson arrays, *Physica D: Nonlinear Phenomena* **74**, 197 (1994).
- [50] E. Ott and T. M. Antonsen, Low dimensional behavior of large systems of globally coupled oscillators, *Chaos: An Interdisciplinary Journal of Nonlinear Science* **18**, 037113 (2008).
- [51] E. Ott and T. M. Antonsen, Long time evolution of phase oscillator systems, *Chaos: An Interdisciplinary Journal of Nonlinear Science* **19**, 023117 (2009).
- [52] Y. Kawamura, H. Nakao, K. Arai, H. Kori, and Y. Kuramoto, Collective Phase Sensitivity, *Physical Review Letters* **101**, 024101 (2008).
- [53] Y. Kawamura, Collective phase dynamics of globally coupled oscillators: Noise-induced anti-phase synchronization, *Physica D: Nonlinear Phenomena* **270**, 20 (2014).
- [54] Y. Kawamura, Collective phase reduction of globally coupled noisy dynamical elements, *Physical Review E* **95**, 032225 (2017).
- [55] Y. Kawamura, H. Nakao, K. Arai, H. Kori, and Y. Kuramoto, Phase synchronization between collective rhythms of globally coupled oscillator groups: Noisy identical case, *Chaos: An Interdisciplinary Journal of Nonlinear Science* **20**, 043109 (2010).
- [56] Y. Kawamura, H. Nakao, K. Arai, H. Kori, and Y. Kuramoto, Phase synchronization between collective rhythms of globally coupled oscillator groups: Noiseless nonidentical case, *Chaos: An Interdisciplinary Journal of Nonlinear Science* **20**, 043110 (2010).
- [57] H. Kori, Y. Kawamura, H. Nakao, K. Arai, and Y. Kuramoto, Collective-phase description of coupled oscillators with general network structure, *Physical Review E* **80**, 036207 (2009).
- [58] Y. Kawamura, Phase synchronization between collective rhythms of fully locked oscillator groups, *Scientific Reports* **4**, 4832 (2014).
- [59] H. Nakao, S. Yasui, M. Ota, K. Arai, and Y. Kawamura, Phase reduction and synchronization of a network of coupled dynamical elements exhibiting collective oscillations, *Chaos: An Interdisciplinary Journal of Nonlinear Science* **28**, 045103 (2018).
- [60] H. Nakao, T. Yanagita, and Y. Kawamura, Phase-Reduction Approach to Synchronization of Spatiotemporal Rhythms in Reaction-Diffusion Systems, *Physical Review X* **4**, 021032 (2014).